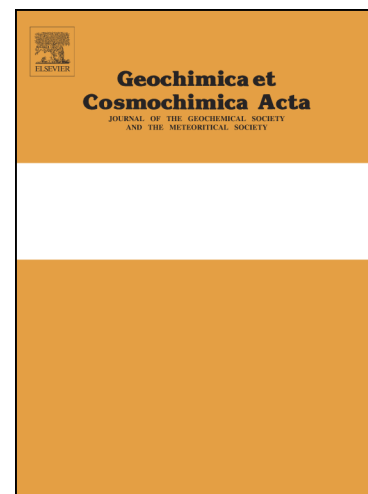


Journal Pre-proofs



An Atomic Force Microscopy Study of Calcite Dissolution in Seawater

Sijia Dong, William M. Berelson, Jess F. Adkins, Nick E. Rollins, John D. Naviaux, Sahand Pirbadian, Mohamed Y. El-Naggar, H. Henry Teng

PII: S0016-7037(20)30358-6
DOI: <https://doi.org/10.1016/j.gca.2020.05.031>
Reference: GCA 11790

To appear in: *Geochimica et Cosmochimica Acta*

Received Date: 8 November 2019
Revised Date: 27 May 2020
Accepted Date: 28 May 2020

Please cite this article as: Dong, S., Berelson, W.M., Adkins, J.F., Rollins, N.E., Naviaux, J.D., Pirbadian, S., El-Naggar, M.Y., Teng, H.H., An Atomic Force Microscopy Study of Calcite Dissolution in Seawater, *Geochimica et Cosmochimica Acta* (2020), doi: <https://doi.org/10.1016/j.gca.2020.05.031>

This is a PDF file of an article that has undergone enhancements after acceptance, such as the addition of a cover page and metadata, and formatting for readability, but it is not yet the definitive version of record. This version will undergo additional copyediting, typesetting and review before it is published in its final form, but we are providing this version to give early visibility of the article. Please note that, during the production process, errors may be discovered which could affect the content, and all legal disclaimers that apply to the journal pertain.

An Atomic Force Microscopy Study of Calcite Dissolution in Seawater

Sijia Dong^{a,b,*}, William M. Berelson^a, Jess F. Adkins^b, Nick E. Rollins^a, John D. Naviaux^b,
Sahand Pirbadian^a, Mohamed Y. El-Naggar^a, H. Henry Teng^c

^a *University of Southern California, Los Angeles, CA, 90089, United States*

^b *California Institute of Technology, Pasadena, CA, 91125, United States*

^c *Institute of Surface Earth System Science, Tianjin University, Tianjin, 300072, China*

* Corresponding author. Email address: dongsj@caltech.edu

Abstract

We present the first examination of calcite dissolution in seawater using Atomic Force Microscopy (AFM). We quantify step retreat velocity and etch pit density to compare dissolution in seawater to low ionic strength water, and also to compare calcite dissolution under AFM conditions to those conducted in bulk solution experiments (e.g. [Subhas et al., 2015](#)). Bulk dissolution rates and step retreat velocities are slower at high and mid-saturation state (Ω) values and become comparable to low ionic strength water rates at low Ω . The onset of defect-assisted etch pit formation in seawater is at $\Omega \sim 0.85$ (defined as Ω_{critical}), higher than in low ionic strength water ($\Omega \sim 0.54$). There is an abrupt increase in etch pit density (from $\sim 10^6 \text{ cm}^{-2}$ to $\sim 10^8 \text{ cm}^{-2}$) occurring when Ω falls below 0.7 in seawater, compared to $\Omega \sim 0.1$ in low ionic strength water, suggesting a transition from defect-assisted dissolution to homogeneous dissolution much closer to equilibrium in seawater. The step retreat velocity (v) does not scale linearly with undersaturation ($1-\Omega$) across an Ω range of 0.4 to 0.9 in seawater, potentially indicating a high

24 order correlation between kink rate and Ω for non-Kossel crystals such as calcite, or surface
25 complexation processes during calcite dissolution in seawater.

26

27

1. INTRODUCTION

28 Calcite plays a critical role in regulating geochemical cycles through dissolution and
29 precipitation in aqueous environments due to the mineral's wide occurrence and high reactivity
30 at earth's surface, (Berner, 1981). For the past three decades, an increasing number of dissolution
31 studies have focused on direct observation and quantification of the kinetics of dissolution on
32 calcite surfaces using microscopic techniques such as AFM (e.g Hillner et al., 1992; Stipp et al.,
33 1994; Dove and Platt, 1996; Liang et al., 1996; Liang and Baer, 1997; McCoy and LaFemina,
34 1997; Shiraki et al., 2000; Lea et al., 2001; Arvidson et al., 2003; Teng, 2004; Bisschop et al.,
35 2006), Vertical Scanning Interferometry (VSI) (e.g. Fischer and Lüttge, 2007; Lüttge and
36 Arvidson, 2010; Smith et al., 2013), X-ray reflectivity (Fenter et al., 2000), X-ray
37 microscopy (Laanait et al., 2015), digital holographic microscopy (Brand et al., 2017), and 3D X-
38 ray microtomography (Noiriel et al., 2019; Yuan et al., 2019). These direct observations have
39 complemented interpretations of results obtained from solution-based bulk calcite dissolution
40 studies (Plummer et al., 1978; Sjöberg and Rickard, 1984; Schott et al., 1989; Gutjahr et al.,
41 1996; Cubillas et al., 2005; Xu et al., 2012), and are now further enhanced by model simulations
42 of molecular-scale processes (Lüttge et al., 2013, 2019), which provide a critical linkage between
43 nanoscale surface observations of crystal dissolution and the phenomenological results at scales
44 of environmental importance.

45 Although the dissolution/precipitation reactions that help regulate atmospheric CO₂ on
46 millennial timescales occur primarily in seawater, all previous AFM and VSI studies have been

47 conducted in simple solutions of low ionic strength by adding chemicals into pure water. Even
48 though the effects of electrolytes, inorganic ions and organic molecules on calcite dissolution
49 have been studied separately to mimic seawater in contact with rock-forming minerals (e.g.
50 Ruiz-Agudo et al., 2009 and 2010; Arvidson et al., 2006; Xu and Higgins, 2010; Klasa et al.,
51 2013; Lea et al., 2001; Vinson et al., 2007; Vinson and Lüttge, 2005; Freij et al., 2004; Kowacz
52 and Putnis, 2008; Teng and Dove, 1997; Perry et al., 2004; Teng et al., 2006; Oelkers et al.,
53 2011), no previous AFM experiment was ever done in seawater itself. However, the discrepancy
54 between calcite dissolution rates in seawater environments and in simple freshwater solutions has
55 long been noticed and has plagued marine chemists for decades. Early dissolution experiments in
56 the ocean water column (Peterson, 1966; Berger, 1967; Honjo and Erez, 1978), and in seawater
57 in the lab (Berner and Morse, 1974; Keir, 1980) reported calcite dissolution rates orders of
58 magnitude lower than those measured in simple solutions (Sjöberg, 1976; Sjöberg and Rickard,
59 1985; Busenberg and Plummer, 1986). Using a ^{13}C labeling technique to determine bulk
60 dissolution rates much more precisely near equilibrium, our group has recently provided the
61 kinetic rate law of calcite dissolution in seawater across the full under-saturation range, and has
62 shown that calcite responds to Ω much differently in seawater than in low ionic strength water
63 (Subhas et al., 2015; Dong et al., 2018; Naviaux et al., 2019). The complicated combination of
64 electrolytes in seawater has a clear effect on the calcite dissolution rate over and above the
65 thermodynamic driving force ($1-\Omega$). However, it is still an open question, whether calcite
66 dissolution in seawater is only the combined effect of individual ionic components, based on the
67 relatively fixed seawater composition, or if complexation between different ionic components
68 add complexity to the dissolution process.

69 This study aims to bridge the seawater and low ionic strength water dissolution studies
70 from an experimental and microscale perspective. Comparisons of solution-based bulk
71 dissolution rates between seawater and low ionic strength water are made, and further explained
72 by AFM observations and quantifications of etch pit origination, densities and step velocities.
73 The values of Ω_{critical} that define transitions between different dissolution mechanisms are
74 identified by the enumeration of etch pit densities. Finally, the correlation of step-retreat velocity
75 against saturation state in seawater is investigated mechanistically.

76

77

2. METHODS

2.1 Sample and solution preparation

79 Calcite {104} surfaces were obtained by using a razor blade to cleave a large crystal of
80 optical-quality Iceland spar. An air burst was then applied to the cleaved fragment
81 (approximately $5 \times 5 \times 0.5$ mm) to remove small adhering particles. The fragment was
82 subsequently adhered to a magnetic plate using double-sided adhesive tape.

83 The experimental solution was standard reference Dickson seawater, Batch 176
84 (https://www.nodc.noaa.gov/ocads/oceans/Dickson_CRM/batches.html) (major chemical
85 composition is shown in Table S1), acidified to desired saturation states by adding HCl. The
86 calcite-undersaturated seawater was kept in gas-impermeable bags with no headspace. Dissolved
87 Inorganic Carbon (DIC) and alkalinity were measured to determine calcite saturation state (Ω ,
88 the ion concentration product over the stoichiometric solubility product). Ω was calculated from
89 the CO2SYS program (Van Heuven et al., 2011) using K'_1 , K'_2 (apparent dissociation constants
90 of carbonic acid in seawater) reported by Mehrbach et al. (1973) and refit by Dickson and
91 Millero (1987); K_{SO_4} reported by Dickson et al. (1990); and borate to salinity ratio reported by

92 Uppström (1974). The uncertainty of Ω was calculated based on the standard errors in DIC and
93 alkalinity as described in Subhas et al. (2015) and averaged ± 0.026 . The determination of Ω is
94 based on the DIC and alkalinity values of the fill bag solution, instead of the outflow solution
95 during dissolution experiments; because there is not enough outflow solution for both
96 measurements during most of our dissolution experiments which last < 1.5 hour.

97

98 **2.2 *In situ* dissolution experiment set-up and AFM imaging**

99 An Asylum Research Cypher ES Environmental Atomic Force Microscope was used to
100 image the calcite dissolution process *in situ*. The fluid cell in this setup (Figure 1) was not a
101 closed chamber but a droplet exposed to the headspace. To maintain the solution chemistry, the
102 headspace air composition was adjusted by adding gas that had a partial pressure of CO_2 in
103 equilibrium with the solution. Two syringes were synchronized to simultaneously inject solutions
104 into and withdraw from the droplet to maintain a constant volume. Alkalinity and DIC
105 measurements of the influent and effluent solution confirmed that Ω remained constant
106 throughout the experiment (Table S2).

107 Dissolution experiments were conducted at 21°C and atmospheric pressure, and real time
108 images were collected in either Tapping or Contact Mode as no obvious difference was observed
109 between the two modes. Numerous commercially available AFM probes we tried corroded
110 within 1~2 hours in seawater, even for Au-coated silicon probes. As the probe corroded, the
111 probe reflectance gradually decreased, and the intensity of the laser beam became too weak to
112 detect. The two types of probes we used for experiments in this paper are: Arrow UHFauD from
113 Asylum Research (<https://afmprobes.asylumresearch.com/arrow-uhfauD.html>), and SNL-10 from
114 Bruker (<https://www.brukerafmprobes.com/p-3693-snl-10.aspx>). Except for the initial

115 experiment that tested the effect of flow rate on step velocity (Figure 2), all experiments
116 afterwards were conducted at a flow rate of 15 mL h⁻¹; at this flow rate, water was in contact
117 with the mineral surface for ≤ 1 minute (residence time).

118

119 **2.3 Determination of step velocity**

120 Due to the non-negligible drifts observed between scans in most of our experiments and
121 the lack of a permanent local reference on the dissolving surface, we elected to use the etch pit
122 widening rates (sum of the edge displacement perpendicular to the acute and obtuse sides) to
123 represent the step retreat speed. The change in etch pits width is the sum of the acute $\langle\bar{4}41\rangle_-$ and
124 obtuse $\langle\bar{4}41\rangle_+$ edges movement. Therefore, measured step speed is the average of the acute and
125 obtuse step velocity. The scan rates for all experiments were either 6.5 Hz or 9.8 Hz, equivalent
126 to 0.2~1.5 $\mu\text{m s}^{-1}$ at the scan sizes used for image collection. This scan rate was significantly
127 faster than the step retreat rates measured in all experiments (0.003~0.4 nm s^{-1}), and therefore
128 should have a negligible influence in generating step velocity error. In addition, all step velocity
129 calculations were made with images of the same scan direction during an experiment (either
130 frame-up or frame-down). Because parallel edges in individual etch pits have opposite polarity
131 ($\langle\bar{4}41\rangle_-$ and $\langle\bar{4}41\rangle_+$), the pit widening rate was therefore the average of the acute and obtuse
132 step retreat velocities. Separate measurements for the acute and obtuse velocities were only made
133 in two dissolution experiments (when image drifting was insignificant) to approximately
134 estimate the ratio of the acute to obtuse velocity during calcite dissolution in seawater.

135 When measuring the step velocities, images were rotated so that the step edges we used
136 to measure pit widths are vertical, and the measurements of pit widths were parallel to the edge
137 motion (Figure 3). Pit widths were only measured at etch pits that have all four edges (indicated

138 by yellow arrows in Figure 3). We excluded etch pits that had coalesced with other etch pits or
 139 long steps (indicated by black arrows in Figure 3).

140 Uncertainty in our measured step velocities was determined as the standard error of a
 141 population of step velocities at 1 to 8 different etch pits and at 2 to 6 different time periods for
 142 each of our 7 experiments (Table 1). Measured step velocity was found to be independent of time
 143 and location (Figure S1), and the variation was largely due to the limited precision in width
 144 measurement within the image analysis program Gwyddion. Specifically, the precision of the
 145 distance measurement was ± 10 nm, whereas step velocities (average of acute and obtuse
 146 velocities) in our experiments were 0.003~0.4 nm s⁻¹ (e.g., every 15 min, the changes in width
 147 were 5~700 nm). Due to the rapid probe corrosion in the experimental seawater, generally
 148 experiments lasted less than 1 h. Therefore, for determinations of widths within several minutes,
 149 especially in slow dissolution experiments, large errors exist because the changes in width are
 150 comparable to the precision of our measurement.

151

152

3. RESULTS

153 **3.1 Effect of flow rate on dissolution and the variation of step velocity on the calcite surface**

154 For etch pits that are one monolayer deep, average step velocities of acute and obtuse
 155 edges vary by as much as 6 times between different etch pits during a single dissolution
 156 experiment at $\Omega = 0.37 \pm 0.01$ (Figure 3). Such variability can only be accounted for by taking
 157 many different measurements. The mean values of average step velocities of the top monolayer
 158 at fluid flow rates of 15 mL h⁻¹, 30 mL h⁻¹, 45 mL h⁻¹ are within one standard deviation of each
 159 other, indicating that dissolution is not limited by diffusion for single monolayers above 15 mL
 160 h⁻¹. Because $\Omega = 0.37 \pm 0.01$ is the lowest saturation state among all dissolution experiments in

161 this study, and step velocity at this saturation is the highest, this experiment would be most
162 sensitive to the impact of our cell and flow design. Since it shows no significant difference in
163 step velocity at the three flow rates, we conclude that all dissolution experiments conducted with
164 flow rates = 15 mL h⁻¹ can be considered surface-controlled instead of diffusion-controlled.
165 Calculated Ω values for the inflow and the outflow solutions, based on DIC and alkalinity
166 measurements, are similar within error (Table S2).

167

168 **3.2 Etch pit morphology in seawater and etch pit density vs. undersaturation**

169 Etch pits in seawater are rhombic with no significant corner rounding observed during
170 dissolution (Figure 3). Dissolution experiments at $\Omega = 0.88 \pm 0.04$ and 0.87 ± 0.04 show no etch
171 pit formation for 30 minutes within the total scanned area of $17.04 \mu\text{m} \times 17.04 \mu\text{m}$, and
172 dissolution only occurs as step retreat of existing edges (Figure 4a). The highest Ω at which etch
173 pit formation is observed is 0.82 ± 0.04 (1 etch pit in $31.9 \mu\text{m}^2$ throughout 60 min). Below $\Omega =$
174 0.82 ± 0.04 , dissolution proceeds in the form of both step retreat and surface pitting (Figure 4b).
175 Etch pit density increases significantly below $\Omega \sim 0.7$, and the rise is used to distinguish the
176 homogeneous etch pit mechanism from the defect-assisted etch pit mechanism, which will be
177 discussed further in Section 4.2.

178

179 **3.3 The dependence of step velocity and dissolution rate on saturation state**

180 Despite the scatter of data points, average step velocity increases as Ω decreases (Figure
181 5, Table 1), with an apparent reaction order $n=2.6$. The scatter results from the variation of step
182 velocities between different etch pits and time periods (Figure 2 and Figure S1), and is also

183 potentially due to the limited precision in etch pit width measurement (see as discussed in
184 Section 2.3).

185 The ratio of obtuse and acute step velocities is determined at $\Omega = 0.46$ and $\Omega = 0.37$,
186 during which experiments no obvious image drift was observed. At two different etch pits in the
187 experiment at $\Omega = 0.46$, $v_{ob}/v_{ac} = 9$ and 5.6 , respectively. At $\Omega = 0.37$, for the continuous
188 spreading of an etch pit, average step velocities at 4 different time intervals give $v_{ob}/v_{ac} = 9.6$.
189 Therefore, our study suggests that calcite dissolution in natural seawater has a v_{ob}/v_{ac} of roughly
190 5 to 10. A more accurate determination of v_{ob}/v_{ac} will require a fixed reference mark on the
191 dissolving surface such as a manually-placed inert feature.

192

193

4. DISCUSSION

194

4.1 Comparison of low ionic strength water studies and seawater

195 Even though the effects of different electrolytes, inorganic ions and organic molecules on
196 calcite dissolution have been widely studied to mimic the reaction in natural aqueous systems
197 such as seawater, all previous AFM and VSI studies were conducted by adding components to
198 deionized water, forming low ionic strength water. In order to investigate the particular effects of
199 individual ions, each component was added separately. Seawater, however, has a combination of
200 assorted ions and the interaction among these species may lead to potentially distinct dissolution
201 phenomena. We summarize some published effects that these components have on calcite
202 dissolution, and discuss whether the concentrations in seawater are comparable to the
203 concentrations needed to affect dissolution behaviors (Table 2).

204 Based on the low ionic strength water studies, various ions and organic matter can affect
205 calcite dissolution by altering etch pit morphology, density, spreading and deepening rate. Etch

206 pit morphology may be altered if acute and obtuse steps are affected differently. Specifically,
207 several studies have reported rounded etch pits with the addition of CO_3^{2-} , PO_4^{3-} , Mn^{2+} and Mg^{2+}
208 (Lea et al., 2001; Vinson et al., 2007; Klasa et al., 2013; Arvidson et al., 2006; Ruiz-Agudo et al.,
209 2009; Xu and Higgins, 2010). While the concentrations of CO_3^{2-} , PO_4^{3-} , and Mn^{2+} in seawater
210 are below the reported values necessary to alter etch pits morphology modification (Table 2), the
211 concentration of Mg^{2+} in seawater is $\sim 0.05 \text{ mol kg}^{-1}$, higher than the reported $[\text{Mg}^{2+}]$ that affects
212 etch pit morphology in Arvidson et al. (2006) ($8 \times 10^{-4} \text{ mol kg}^{-1}$), albeit lower than the
213 concentration in Ruiz-Agudo et al. (2009) (1 mol kg^{-1}). Nevertheless, our results of calcite etch
214 pit morphology in seawater show no obvious difference than previously published freshwater
215 morphology (Figure 3).

216 In addition to etch pit morphology, Mg^{2+} , SO_4^{2-} and PO_4^{3-} are also suggested to increase
217 the density of etch pits nucleated on calcite surfaces (Ruiz-Agudo et al., 2009; Klasa et al., 2013).
218 Meanwhile, CO_3^{2-} , Mn^{2+} , Sr^{2+} , NH_4^+ , Mg^{2+} , and SO_4^{2-} are supposed to decrease step velocities
219 during calcite dissolution (Lea et al., 2001; Klasa et al., 2013; Ruiz-Agudo et al., 2009).
220 However, only $[\text{Mg}^{2+}]$ and $[\text{Sr}^{2+}]$ in seawater are higher than the concentrations required for the
221 effects as reported in the literature, and the effect of Sr^{2+} on step velocity is small (Lea et al.,
222 2001) (comparable to the error bars) (Table 2). Therefore, the combination of the ions in
223 seawater, especially Mg^{2+} , may have a dual and opposing effect on calcite dissolution – the
224 promotion of etch pit nucleation and the inhibition of etch pit spreading velocity. The
225 comparison of etch pit density and step velocity between calcite dissolution in low ionic strength
226 water and seawater will be discussed in detail in the following sections.

227

228 4.2 Etch pit density and the identification of changes in dissolution mechanisms

229 Solution-based bulk dissolution rates (Figure 6a) show different dependencies on
230 saturation state in low ionic strength water and seawater. These separate behaviors are likely the
231 combined effect of the different responses of etch pit density (Figure 6b) and step velocity
232 (Figure 6c) to the solution saturation state. Near equilibrium, solution-based rates in seawater are
233 lower than in low ionic strength water by 2-4 orders of magnitude. But the two rates become
234 comparable at $\Omega < 0.6$ (Figure 6a). In this section, AFM-determined etch pit density is used to
235 identify which dissolution mechanisms dominate across a wide range of Ω values and to
236 compare the Ω_{critical} s at which the mechanism changes between seawater and low ionic strength
237 water (Figure 6b).

238 Distinct dissolution mechanisms at different saturation states in low ionic water have
239 been both theoretically proposed and experimentally identified (Holdren and Berner, 1979;
240 Brantley et al., 1986; Gratz et al., 1991; Stipp et al., 1994; Lasaga and Lüttge, 2001; Teng, 2004;
241 Dove et al., 2005; Arvidson and Lüttge, 2010). Proceeding from near-equilibrium to farther from
242 equilibrium, dissolution occurs as (1) retreat of pre-existing steps at edges, corners and
243 dislocations; (2) opening of etch pits at defects; and finally (3) opening of etch pits
244 homogeneously across the mineral surface. After formation, etch pits can either spread as “2D
245 pancakes” (Dove et al, 2005), or “step-waves” that contain multiple layers (Lasaga and Lüttge,
246 2001). The transitions between different dissolution mechanisms happen at Ω_{critical} , and imply a
247 discontinuous relationship between rate and undersaturation.

248 The determination of Ω_{critical} in bulk dissolution experiments (Subhas et al., 2017; Dong
249 et al., 2018; Naviaux et al., 2019) is done by fitting dissolution rates to a mechanistic model
250 (Dove et al, 2005) and identifying the breaks in slope in a plot of rate vs. undersaturation. We set
251 out to determine if these transitions in mechanism can be verified by AFM observations.

252 Assuming the onset of the defect-assisted etch pit mechanism is marked by the highest Ω
253 observed for etch pit formation, and the onset of the homogeneous etch pit mechanism is
254 revealed by a precipitous increase of pit density as Ω falls below a critical value, [Teng \(2004\)](#)
255 measured pit densities against solution undersaturation in weak electrolyte solutions. This work
256 showed an increase of pit densities as Ω falls, and a very rapid rise at $\Omega = 0.007$, as pit density
257 increases from $4 \times 10^6 \text{ cm}^{-2}$ to $5 \times 10^8 \text{ cm}^{-2}$ ([Teng, 2004](#)). Compared to the observations in weak
258 electrolyte solutions, we have previously reported Ω_{critical} for the opening of defect-assisted etch
259 pits in seawater is $\Omega = 0.9$ (versus $\Omega = 0.54$ in low ionic strength water), and the Ω_{critical} for
260 homogeneous etch pit formation at $\Omega = 0.75$ (versus $\Omega = 0.007$ in low ionic strength water) in
261 bulk dissolution experiments ([Naviaux et al., 2019](#)).

262 The AFM measurements generally support our earlier reported Ω_{critical} values in seawater.
263 No etch pits are observed during dissolution experiments at $\Omega = 0.87$ and 0.88 ; dissolution only
264 occurs as step retreat (Figure 4a). The highest Ω observed for etch pit formation is 0.82 , with a
265 pit density of $3.1 \times 10^6 \text{ cm}^{-2}$ (Figure 6b, Table 4). The transition between step retreat and defect-
266 assisted etch pit mechanisms is therefore between 0.82 and 0.87 (red solid line in Figure 6c),
267 comparable to $\Omega_{\text{critical}} = 0.87$ in [Dong et al. \(2018\)](#) and 0.9 in [Naviaux et al. \(2019\)](#). Below $\Omega =$
268 0.7 , pit density increases abruptly to $\sim 10^8 \text{ cm}^{-2}$ (Figure 6c), similar to the pit density reported for
269 homogeneous etch pit formation mechanism far from equilibrium in [Teng \(2004\)](#) ($n_s = 10^8$ sites
270 cm^{-2}) and in [Ruiz-Agudo et al. \(2009\)](#) ($n_s = 10^9$ sites cm^{-2}). The significant difference in etch pit
271 density above and below $\Omega = 0.7$ (red dashed line in Figure 6c) in seawater indicates the onset of
272 the homogeneous etch pit formation mechanism, which also agrees with the corresponding
273 $\Omega_{\text{critical}} = 0.75$ proposed by [Naviaux et al. \(2019\)](#). The fact that the onsets of both defect-assisted
274 and homogeneous etch pit mechanisms occur at higher Ω in seawater (red solid and dashed lines

275 in Figure 6c) than in low ionic strength water (black solid and dashed lines in Figure 6c) is
276 demonstrated in both solution-based experiments and this AFM work. This basic result implies
277 that the surface energy of calcite is lower in seawater than it is in low ionic strength water. Based
278 on the slopes of our bulk dissolution rate data in the 2D etch pit mode, we diagnosed a surface
279 energy of $\sim 34 \text{ mJ m}^{-2}$ (Naviaux et al., 2019), while the reported freshwater value is almost three
280 times higher at 97 mJ m^{-2} (Lasaga, 1998; Steefel and Van Cappellen, 1990).

281 The offset in Ω_{critical} between seawater and low ionic strength solutions, and the
282 implication of surface energy lowering, could be related to the effects of other ions besides Ca^{2+}
283 and CO_3^{2-} (e.g. Mg^{2+} , SO_4^{2-} etc.) on etch pit density. Although the effects of these ions have yet
284 to be carefully tested in seawater near equilibrium, AFM studies and molecular dynamics
285 simulations in simple solutions suggest several potential mechanisms. Mg^{2+} has been reported to
286 increase the density and depth of etch pits nucleated on calcite surfaces at concentrations above
287 0.05 mol kg^{-1} far from equilibrium (Ruiz-Agudo et al., 2009). A molecular dynamics (MD)
288 simulation by Kerisit and Parker (2004) has shown that Mg^{2+} is able to attract water molecules
289 from the calcite surface to retain a full coordination shell (i.e. 6 water molecules) once it adsorbs
290 as an inner-sphere complex directly above a surface carbonate group. As a result, water
291 molecules could be transferred from surface calcium sites on calcite during magnesium
292 adsorption. Such a strong magnesium-surface interaction and the fact that magnesium can disrupt
293 the surface hydration layer can lead to surface destabilization, and ultimately favor nucleation of
294 etch pits. A reduction in the kinetic barrier associated with the magnesium-calcite surface
295 interaction initiates etch pit nucleation which manifests itself as an increase in etch pit density.

296 In addition to Mg^{2+} , SO_4^{2-} has also been reported to increase the etch pit deepening rate
297 and etch pit density during calcite dissolution in simple ionic solutions (Ruiz-Agudo et al., 2009).

298 One possible explanation of the SO_4^{2-} effect is via an increase in Mg-adsorption on carbonates.
299 Specifically, the rate limiting step for Mg^{2+} adsorption onto carbonates is its dehydration
300 (Lippmann, 1973), and SO_4^{2-} is known to enhance cation desolvation through the formation of
301 ion pairs (Piana et al., 2006). As a result, Mg^{2+} and SO_4^{2-} hydrated ions in the solution combine
302 to form double solvent separated ion pairs or contact ion pairs (Rudolph et al., 2004), and water
303 molecules are lost from such complexes. Dehydrated Mg^{2+} ions are then available to adsorb on
304 carbonates. In this respect, Brady et al. (1996) have also shown that adsorption of magnesium on
305 carbonates is enhanced in sulfate-rich solutions during dolomite growth. These previous studies
306 suggest a potential SO_4^{2-} effect on etch pit formation during calcite dissolution. However, these
307 mechanisms are based upon studies conducted in simpler ionic solutions than seawater and at Ω
308 values far from equilibrium. An important next step is to investigate how the two negatively
309 charged species, SO_4^{2-} and CO_3^{2-} , might compete for surface complexation sites on calcite in
310 seawater, and how this competition might be affected by the presence of Mg^{2+} .

311

312 **4.3 Dependence of step velocity on the saturation state**

313 Solution-based bulk mineral dissolution rate and step velocity show similar patterns in
314 how they differ between seawater and low ionic strength water, with rates being lower in
315 seawater near equilibrium but similar far from equilibrium (Figure 6a and 6c). For the
316 comparison of step velocity, however, it is worth noting that most freshwater studies were
317 conducted at extremely low saturation states, and the only study conducted at high Ω was aimed
318 at conditions of geological carbon sequestration, and thus had high temperature (Xu et al., 2010).
319 These authors showed that step velocities are smaller at lower temperature. However, because

320 there is only one data point at 50 °C between $\Omega = 0.5$ and 1 in [Xu et al. \(2010\)](#), it is difficult to
 321 extrapolate the high temperature velocities to 21 °C at near equilibrium conditions.

322 In surface nucleation and spiral growth models, the speed of a moving step, v , is related
 323 to the kinetic coefficient β and the solution saturation state Ω via ([Chernov, 1984; Malkin et al.,](#)
 324 [1989](#)):

$$v = \omega\beta C_e(1 - \Omega)$$

Eq. 1

327 where ω is the molecular volume of a molecule in the crystal ($6.12 \times 10^{-29} \text{ m}^3 \text{ molecule}^{-1}$), and
 328 C_e is the mineral solubility ($2.59 \times 10^{22} \text{ atoms m}^{-3}$). The same mechanistic model has been
 329 suggested to work for quartz dissolution by analogous processes ([Dove et al., 2005](#)). For
 330 dissolution, the kinetic coefficient β depends on temperature and the activation energy of
 331 detachment from steps (ϵ_{step}) during step retreat:

$$\beta = \beta_0 \exp\left(-\frac{\epsilon_{step}}{k_b T}\right)$$

Eq. 2

334 where k_b is Boltzmann's constant, T is temperature (Kelvin). At pre-existing steps or after an
 335 etch pit is initiated, dissolution occurs as the step retreats and therefore β should remain constant
 336 during dissolution. As a result, v (measurable on AFM) will be a linear function of Ω at a given
 337 temperature. However, these models were developed for Kossel crystals or for AB crystals
 338 where the anion and the cation exist in solution in their solid stoichiometric ratio. Here we
 339 address whether calcite dissolution in seawater still has a linear dependence of step velocity on Ω ,
 340 that is to say a constant kinetic coefficient, β .

341 Previous calcite dissolution experiments in low ionic strength solutions showed a
342 generally linear dependence of step velocity on saturation state below $\Omega = 0.8$, but the linear
343 trend fell off near equilibrium (Xu et al., 2010). In addition, our group has consistently reported a
344 highly nonlinear dependence of bulk dissolution rate on saturation state in seawater (Subhas et
345 al., 2015; Dong et al., 2018; Naviaux et al., 2019). Because it is still an open question whether
346 Eq.1 applies, we use β^* to describe the measured quantity, $v / \{\omega C_e(1 - \Omega)\}$.

347 In our group's previous study, where we used the mechanistic framework in Dove et al.
348 (2005) to identify transitions of dissolution mechanisms based on bulk rate measurements
349 (Naviaux et al., 2019), we assumed a constant β^* across Ω values within the homogeneous etch
350 pit spreading mechanism and the defect-assisted etch pit mechanism, and that there was a
351 different β^* for the step retreat mechanism. Under the assumption that Eq. 1 held true, Naviaux
352 et al. were able to fit their bulk dissolution data from $0 < \Omega < 0.9$ (defect-assisted and
353 homogenous etch pit formation) using a $\beta^* = 5 \times 10^{-3} \text{ m s}^{-1}$, and from $0.9 < \Omega < 1$ (step
354 propagation) with a much smaller value of $\beta^* = 3 \times 10^{-7} \text{ m s}^{-1}$. The authors noted that, when
355 extrapolating to $\Omega = 0$, the β^* of $5 \times 10^{-3} \text{ m s}^{-1}$ implied a relatively fast upper limit of v of $\sim 10 \text{ nm}$
356 s^{-1} at 21°C in seawater.

357 Direct measurements of step velocities using AFM allow us to calculate the “kinetic
358 coefficient” without making assumptions about the etch pit density (n_s) and the independence of
359 β^* on Ω within the same dissolution mechanism, as was done for Naviaux et al. (2019). AFM-
360 determined step velocities in this work are not linear with saturation states (Figure 5, slope >1 in
361 the log-log plot). Upon measuring the mean step velocity of acute and obtuse steps, the mean
362 “kinetic coefficient” for the two types of edges can be calculated at different saturation states.
363 Note that because we use etch pit widening rates to calculate step velocity, the β^* s we obtain are

364 only between $0 < \Omega < 0.9$, for homogenous 2D dissolution and defect-assisted dissolution. Our
 365 results show a variable β^* across an Ω range of 0.4 to 0.9 in seawater, with significantly higher
 366 values at lower Ω (Figure 7). From near equilibrium to $\Omega = 0.4$, β^* increases from $1.4 \times 10^{-5} \text{ m s}^{-1}$
 367 to $3.9 \times 10^{-4} \text{ m s}^{-1}$. An extrapolation to $\Omega = 0$ suggests an upper limit for average acute and
 368 obtuse step velocity of $\sim 1 \text{ nm s}^{-1}$ (Figure 5), an order of magnitude lower than the value derived
 369 from bulk rate measurements in [Naviaux et al. \(2019\)](#). This offset between observed and
 370 calculated values shows that the surface nucleation/dissolution models (i.e., [Chernov, 1984](#);
 371 [Malkin et al., 1989](#); [Dove et al, 2005](#)) may be incomplete for calcite dissolution in seawater.

372 One possible reason that may account for the nonlinear dependence of step velocity on Ω
 373 for calcite dissolution in seawater is that the linear relationship is derived using a Kossel crystal
 374 model ([Kossel, 1927](#); [Stranski, 1928](#)) containing only one type of growth unit (e.g. quartz SiO_2
 375 in [Dove et al., 2005](#)), whereas calcite is a non-Kossel crystal and seawater has a variable and
 376 large ratio of $\text{Ca}:\text{CO}_3$. The derivation of the linear relationship links the step velocity (v) to the
 377 motion of a single kink along the step (v_k), which is further related to the difference between the
 378 rates of attachment (j^+) and detachment (j^-) of the growth unit ([Qiu and Orme, 2008](#)). The
 379 attachment and detachment rates are directly related to the chemical potentials of the starting and
 380 activated states, and therefore kink mobility (j^\pm) is a linear function of Ω . In the limit of
 381 infinitely long steps with growth occurring via attachment and detachment at kink sites, and
 382 under the further assumption that nucleation of kink sites is not rate limiting, v can be related to
 383 the v_k by

$$384 \quad v = b_\perp * \rho_k * v_k$$

385 Eq. 3

386 where b_{\perp} is the molecular distance in the direction of the step motion (or perpendicular to the
387 step edge) and ρ_k is the kink density. When kink-nucleation and supersaturation dependent
388 effects are negligible compared to kinks produced by thermal fluctuations, the kink density may
389 be expressed as a constant (Chernov, 2004; Chernov et al., 2004). This assumption leads to the
390 common expression of a linear dependence of step velocity on saturation state (Eq. 1) for a
391 Kossel crystal model.

392 However, for non-Kossel crystals, there are different j^{\pm} s when growth/dissolution
393 requires incorporation/detachment of alternating ions (e.g. Ca^{2+} and CO_3^{2-} for calcite). As a result
394 of a cooperative interaction of different ions within the unit cell, the linear dependence of the
395 kink velocity (v_k) on the saturation state will no longer hold true (Chernov, 2004; Zhang and
396 Nancollas, 1998; Qiu and Orme 2008; Nehrke et al., 2007; Stack and Grantham, 2010; Wolthers
397 et al., 2012; Nielsen et al., 2012). For calcite dissolution, specifically, mechanistic models
398 suggest different site-specific reactions with different rate constants at the $>\text{CO}_3^-$ and $>\text{Ca}^+$ sites
399 of the calcite surface (Arakaki and Mucci, 1995), which also imply different j^{\pm} s at the kink sites.
400 This proposed mechanism in low ionic strength water will be altered by the complexation of
401 surface sites from the major ions present in seawater (Ding and Rahman, 2018; Song et al., 2017).

402 In addition to different j^{\pm} s for non-Kossel crystal, another reason that may cause the
403 non-linearity in the step velocity vs. Ω is the change of chemical potential due to the surface
404 complexation processes between calcite and the ions in seawater. This statement is supported by
405 the fact that the linearity between step velocity vs. Ω is higher in low ionic strength water (Xu et
406 al., 2010) than in seawater (this study). In addition, the surface nucleation/dissolution models
407 also do not permit an analysis of how solution stoichiometry may affect crystal growth and
408 dissolution in the presence of non-lattice ions which may disturb the movement of lattice cations

409 and anions (Zhang and Nancollas 1998). Whereas a complexation model that couples the effects
410 of Ω with the speciation of the solution and mineral surface successfully describes calcite
411 dissolution rates via defect-assisted etch pit formation in seawater (Naviaux, 2020).

412 To sum up, even though applying the mechanistic framework of the surface
413 nucleation/dissolution models (i.e., Chernov, 1984; Malkin et al., 1989; Dove et al, 2005) to
414 dissolution rate measurements has proved successful in identifying transitions in mechanisms
415 (Ω_{critical}) (Section 4.2), and the activation energy for crystallization and dissolution (Van
416 Driessche et al., 2010; Naviaux et al., 2019), the linear correlation between step velocity and
417 saturation state may not apply for calcite dissolution in seawater. The possible mechanisms for
418 the nonlinearity are the different attachment and detachment rates (j^{\pm}) for the alternating ions in
419 non-Kossel crystals, and the surface complexation processes between the crystal and the ions in
420 seawater.

421

422 5. CONCLUSIONS

423 We report AFM observations of calcite dissolution in seawater for the first time and show
424 no significant difference of etch pit morphology between dissolution in seawater and low ionic
425 strength water – both are rhombic with no significant corner rounding. The ratio of obtuse to
426 acute step velocity is 5-10 in seawater. Solution-based bulk dissolution rate is 2-4 orders of
427 magnitude lower in seawater than in low ionic strength water near equilibrium, but more
428 comparable far from equilibrium. The different responses of dissolution rates to Ω between the
429 two water types are a combined effect of different etch pit densities and step velocities. Even
430 though the dominating dissolution mechanisms and the etch pit densities within the
431 homogeneous etch pit spreading mechanism are the same between seawater and low ionic

432 strength water, the transitions of dissolution mechanisms occur at much higher Ω in seawater,
433 implying a lower surface energy for calcite in seawater than in low ionic strength water. The
434 promotion of etch pit formation in seawater agrees with previously published effect of Mg^{2+} in
435 simple solutions. Although etch pit opening is enhanced, step retreat is inhibited at high and mid-
436 undersaturation states in seawater compared to low ionic strength water, leading to net lower
437 bulk dissolution rates near equilibrium. Step velocities do not depend linearly on Ω in seawater,
438 potentially due to the different attachment and detachment rates for the alternating ions in non-
439 Kossel crystals and the surface complexation processes between the crystal and the ions in
440 seawater.

441

442

443 **ACKNOWLEDGEMENTS**

444 This work was supported by NSF Ocean Acidification grants (numbers OCE1220600 and
445 OCE1220302), USC Dornsife Doctoral Fellowship, and Grantham Foundation at Caltech. The
446 authors would like to thank four anonymous journal reviewers, as well as the associate editor Dr.
447 Oleg Pokrovsky, for their insightful comments and suggestions that helped to improve this
448 manuscript. We thank Mina Hong, Zibo Li and Liang Zhao for helpful discussions on AFM
449 operations. We also thank Josh West for his suggestions on the manuscript.

450

451 **REFERENCES**

452

453 Arakaki, T., & Mucci, A. (1995). A continuous and mechanistic representation of calcite
454 reaction-controlled kinetics in dilute solutions at 25 C and 1 atm total pressure. *Aquatic*
455 *Geochemistry*, 1(1), 105-130.

- 456 Arvidson, R. S., & Lüttge, A. (2010). Mineral dissolution kinetics as a function of distance from
457 equilibrium—New experimental results. *Chemical Geology*, 269(1-2), 79-88.
- 458 Arvidson, R. S., Collier, M., Davis, K. J., Vinson, M. D., Amonette, J. E., & Lüttge, A. (2006).
459 Magnesium inhibition of calcite dissolution kinetics. *Geochimica et Cosmochimica*
460 *Acta*, 70(3), 583-594.
- 461 Arvidson, R. S., Ertan, I. E., Amonette, J. E., & Lüttge, A. (2003). Variation in calcite
462 dissolution rates: A fundamental problem?. *Geochimica et cosmochimica acta*, 67(9),
463 1623-1634.
- 464 Berger, W. H. (1977). Deep-sea carbonate and the deglaciation preservation spike in pteropods
465 and foraminifera. *Nature*, 269(5626), 301-304.
- 466 Berner, R. A. (1981). Kinetics of weathering and diagenesis. *Rev. Mineral.:(United States)*, 8.
- 467 Berner, R. A., & Morse, J. W. (1974). Dissolution kinetics of calcium carbonate in sea water; IV,
468 Theory of calcite dissolution. *American Journal of Science*, 274(2), 108-134.
- 469 Bisschop, J., Dysthe, D. K., Putnis, C. V., & Jamtveit, B. (2006). *In situ* AFM study of the
470 dissolution and recrystallization behaviour of polished and stressed calcite
471 surfaces. *Geochimica et cosmochimica acta*, 70(7), 1728-1738.
- 472 Brady, P. V., Krumhansl, J. L., & Papenguth, H. W. (1996). Surface complexation clues to
473 dolomite growth. *Geochimica et Cosmochimica Acta*, 60(4), 727-731.
- 474 Brand, A. S., Feng, P., & Bullard, J. W. (2017). Calcite dissolution rate spectra measured by *in*
475 *situ* digital holographic microscopy. *Geochimica et cosmochimica acta*, 213, 317-329.
- 476 Brantley, S. L., Crane, S. R., Crerar, D. A., Hellmann, R., & Stallard, R. (1986). Dissolution at
477 dislocation etch pits in quartz. *Geochimica et Cosmochimica Acta*, 50(10), 2349-2361.
- 478 Busenberg, E., Plummer, L. N., & Mumpton, F. A. (1986). A comparative study of the
479 dissolution and crystal growth kinetics of calcite and aragonite. *Studies Diagenesis USGS*
480 *Bull*, 1578, 139-168.
- 481 Chernov A.A. (1984). *Modern Crystallography III: Crystal Growth*. Springer Science &
482 Business Media.
- 483 Chernov, A. A. (2004). Notes on interface growth kinetics 50 years after Burton, Cabrera and
484 Frank. *Journal of Crystal Growth*, 264(4), 499-518.
- 485 Chernov, A. A., De Yoreo, J. J., Rashkovich, L. N., & Vekilov, P. G. (2004). Step and kink
486 dynamics in inorganic and protein crystallization. *MRS bulletin*, 29(12), 927-934.

- 487 Cubillas, P., Köhler, S., Prieto, M., Chaïrat, C., & Oelkers, E. H. (2005). Experimental
488 determination of the dissolution rates of calcite, aragonite, and bivalves. *Chemical*
489 *Geology*, 216(1-2), 59-77.
- 490 De Giudici, G. (2002). Surface control vs. diffusion control during calcite dissolution:
491 Dependence of step-edge velocity upon solution pH. *American Mineralogist*, 87(10),
492 1279-1285.
- 493 Dickson, A. G., & Millero, F. J. (1987). A comparison of the equilibrium constants for the
494 dissociation of carbonic acid in seawater media. *Deep Sea Research Part A.*
495 *Oceanographic Research Papers*, 34(10), 1733-1743.
- 496 Dickson, A. G., Wesolowski, D. J., Palmer, D. A., & Mesmer, R. E. (1990). Dissociation
497 constant of bisulfate ion in aqueous sodium chloride solutions to 250. degree. C. *Journal*
498 *of Physical Chemistry*, 94(20), 7978-7985.
- 499 Ding, H., & Rahman, S. R. (2018). Investigation of the Impact of Potential Determining Ions
500 from Surface Complexation Modeling. *Energy & Fuels*, 32(9), 9314-9321.
- 501 Dong, S., Berelson, W. M., Rollins, N. E., Subhas, A. V., Naviaux, J. D., Celestian, A. J., ... &
502 Adkins, J. F. (2019). Aragonite dissolution kinetics and calcite/aragonite ratios in sinking
503 and suspended particles in the North Pacific. *Earth and Planetary Science Letters*, 515, 1-
504 12.
- 505 Dong, S., Subhas, A. V., Rollins, N. E., Naviaux, J. D., Adkins, J. F., & Berelson, W. M. (2018).
506 A kinetic pressure effect on calcite dissolution in seawater. *Geochimica et Cosmochimica*
507 *Acta*, 238, 411-423.
- 508 Dove, P. M., & Platt, F. M. (1996). Compatible real-time rates of mineral dissolution by atomic
509 force microscopy (AFM). *Chemical Geology*, 127(4), 331-338.
- 510 Dove, P. M., Han, N., & De Yoreo, J. J. (2005). Mechanisms of classical crystal growth theory
511 explain quartz and silicate dissolution behavior. *Proceedings of the National Academy of*
512 *Sciences*, 102(43), 15357-15362.
- 513 Fenter, P., Geissbühler, P., DiMasi, E., Srajer, G., Sorensen, L. B., & Sturchio, N. C. (2000).
514 Surface speciation of calcite observed in situ by high-resolution X-ray
515 reflectivity. *Geochimica et Cosmochimica Acta*, 64(7), 1221-1228.

- 516 Fischer, C., & Lüttge, A. (2007). Converged surface roughness parameters—a new tool to
517 quantify rock surface morphology and reactivity alteration. *American Journal of*
518 *Science*, 307(7), 955-973.
- 519 Freij, S. J., Putnis, A., & Astilleros, J. M. (2004). Nanoscale observations of the effect of cobalt
520 on calcite growth and dissolution. *Journal of Crystal Growth*, 267(1-2), 288-300.
- 521 Gratz, A. J., Manne, S., & Hansma, P. K. (1991). Atomic force microscopy of atomic-scale
522 ledges and etch pits formed during dissolution of quartz. *Science*, 251(4999), 1343-1346.
- 523 Gutjahr, A., Dabringhaus, H., & Lacmann, R. (1996). Studies of the growth and dissolution
524 kinetics of the CaCO₃ polymorphs calcite and aragonite I. Growth and dissolution rates in
525 water. *Journal of crystal growth*, 158(3), 296-309.
- 526 Harstad, A. O., & Stipp, S. L. S. (2007). Calcite dissolution: Effects of trace cations naturally
527 present in Iceland spar calcites. *Geochimica et Cosmochimica Acta*, 71(1), 56-70.
- 528 Hillner, P. E., Gratz, A. J., Manne, S., & Hansma, P. K. (1992). Atomic-scale imaging of calcite
529 growth and dissolution in real time. *Geology*, 20(4), 359-362.
- 530 Holdren Jr, G. R., & Berner, R. A. (1979). Mechanism of feldspar weathering—I. Experimental
531 studies. *Geochimica et Cosmochimica Acta*, 43(8), 1161-1171.
- 532 Honjo, S., & Erez, J. (1978). Dissolution rates of calcium carbonate in the deep ocean; an in-situ
533 experiment in the North Atlantic Ocean. *Earth and Planetary Science Letters*, 40(2), 287-
534 300.
- 535 Keir, R. S. (1980). The dissolution kinetics of biogenic calcium carbonates in
536 seawater. *Geochimica et Cosmochimica Acta*, 44(2), 241-252.
- 537 Kerisit, S., & Parker, S. C. (2004). Free energy of adsorption of water and metal ions on the
538 {1014} calcite surface. *Journal of the American Chemical Society*, 126(32), 10152-10161.
- 539 Klasa, J., Ruiz-Agudo, E., Wang, L. J., Putnis, C. V., Valsami-Jones, E., Menneken, M., &
540 Putnis, A. (2013). An atomic force microscopy study of the dissolution of calcite in the
541 presence of phosphate ions. *Geochimica et Cosmochimica Acta*, 117, 115-128.
- 542 Kossel, W. (1927). Zur theorie des kristallwachstums. *Nachrichten von der Gesellschaft der*
543 *Wissenschaften zu Göttingen, Mathematisch-Physikalische Klasse*, 1927, 135-143.
- 544 Kowacz, M., & Putnis, A. (2008). The effect of specific background electrolytes on water
545 structure and solute hydration: Consequences for crystal dissolution and
546 growth. *Geochimica et Cosmochimica Acta*, 72(18), 4476-4487.

- 547 Laanait, N., Callagon, E. B., Zhang, Z., Sturchio, N. C., Lee, S. S., & Fenter, P. (2015). X-ray–
548 driven reaction front dynamics at calcite-water interfaces. *Science*, 349(6254), 1330-1334.
- 549 Lasaga, A. C., & Lüttge, A. (2001). Variation of crystal dissolution rate based on a dissolution
550 stepwave model. *Science*, 291(5512), 2400-2404.
- 551 Lasaga, A.C. (1998). Kinetic Theory in the Earth Sciences. Princeton University Press.
- 552 Lea, A. S., Amonette, J. E., Baer, D. R., Liang, Y., & Colton, N. G. (2001). Microscopic effects
553 of carbonate, manganese, and strontium ions on calcite dissolution. *Geochimica et*
554 *Cosmochimica Acta*, 65(3), 369-379.
- 555 Liang, Y., & Baer, D. R. (1997). Anisotropic dissolution at the CaCO₃ (1014)—water
556 interface. *Surface Science*, 373(2-3), 275-287.
- 557 Liang, Y., Baer, D. R., McCoy, J. M., Amonette, J. E., & Lafemina, J. P. (1996). Dissolution
558 kinetics at the calcite-water interface. *Geochimica et Cosmochimica Acta*, 60(23), 4883-
559 4887.
- 560 Lippmann F. (1973) Sedimentary Carbonate Minerals. Springer-Verlag, Berlin.
- 561 Lüttge, A., & Arvidson, R. S. (2010). Reactions at surfaces: A new approach integrating
562 interferometry and kinetic simulations. *Journal of the American Ceramic Society*, 93(11),
563 3519-3530.
- 564 Lüttge, A., Arvidson, R. S., & Fischer, C. (2013). A stochastic treatment of crystal dissolution
565 kinetics. *Elements*, 9(3), 183-188.
- 566 Lüttge, A., Arvidson, R. S., Fischer, C., & Kurganskaya, I. (2019). Kinetic concepts for
567 quantitative prediction of fluid-solid interactions. *Chemical Geology*, 504, 216-235.
- 568 Malkin, A. I., Chernov, A. A., & Alexeev, I. V. (1989). Growth of dipyramidal face of
569 dislocation-free ADP crystals; free energy of steps. *Journal of Crystal Growth*, 97(3-4),
570 765-769.
- 571 McCoy, J. M., & LaFemina, J. P. (1997). Kinetic Monte Carlo investigation of pit formation at
572 the CaCO₃ (1014) surface-water interface. *Surface Science*, 373(2-3), 288-299.
- 573 Mehrbach, C., Culberson, C. H., Hawley, J. E., & Pytkowicz, R. M. (1973). Measurement of the
574 apparent dissociation constants of carbonic acid in seawater at atmospheric
575 pressure. *Limnology and Oceanography*, 18(6), 897-907.
- 576 Morse, J. W., & Berner, R. A. (1972). Dissolution kinetics of calcium carbonate in sea water; I,
577 A kinetic origin for the lysocline. *American Journal of Science*, 272(9), 840-851.

- 578 Naviaux, J. D. (2020). Chemical and Physical Mechanisms of Calcite Dissolution in
579 Seawater (Doctoral dissertation, California Institute of Technology).
- 580 Naviaux, J. D., Subhas, A. V., Rollins, N. E., Dong, S., Berelson, W. M., & Adkins, J. F. (2019).
581 Temperature dependence of calcite dissolution kinetics in seawater. *Geochimica et*
582 *Cosmochimica Acta*, 246, 363-384.
- 583 Nehrke, G., Reichart, G. J., Van Cappellen, P., Meile, C., & Bijma, J. (2007). Dependence of
584 calcite growth rate and Sr partitioning on solution stoichiometry: non-Kossel crystal
585 growth. *Geochimica et Cosmochimica Acta*, 71(9), 2240-2249.
- 586 Nielsen, L. C., DePaolo, D. J., & De Yoreo, J. J. (2012). Self-consistent ion-by-ion growth
587 model for kinetic isotopic fractionation during calcite precipitation. *Geochimica et*
588 *Cosmochimica Acta*, 86, 166-181.
- 589 Noiriél, C., Oursin, M., Saldi, G., & Habberthür, D. (2018). Direct determination of dissolution
590 rates at crystal surfaces using 3D X-ray microtomography. *ACS Earth and Space*
591 *Chemistry*, 3(1), 100-108.
- 592 Oelkers, E. H., Golubev, S. V., Pokrovsky, O. S., & Bénézech, P. (2011). Do organic ligands
593 affect calcite dissolution rates?. *Geochimica et Cosmochimica Acta*, 75(7), 1799-1813.
- 594 Perry IV, T. D., Duckworth, O. W., McNamara, C. J., Martin, S. T., & Mitchell, R. (2004).
595 Effects of the biologically produced polymer alginic acid on macroscopic and
596 microscopic calcite dissolution rates. *Environmental science & technology*, 38(11), 3040-
597 3046.
- 598 Peterson, M. N. A. (1966). Calcite: rates of dissolution in a vertical profile in the central
599 Pacific. *Science*, 154(3756), 1542-1544.
- 600 Piana, S., Jones, F., & Gale, J. D. (2006). Assisted desolvation as a key kinetic step for crystal
601 growth. *Journal of the American Chemical Society*, 128(41), 13568-13574.
- 602 Plummer, L. N., Wigley, T. M. L., & Parkhurst, D. L. (1978). The kinetics of calcite dissolution
603 in CO₂-water systems at 5 degrees to 60 degrees C and 0.0 to 1.0 atm CO₂. *American*
604 *journal of science*, 278(2), 179-216.
- 605 Qiu, S. R., & Orme, C. A. (2008). Dynamics of biomineral formation at the near-molecular
606 level. *Chemical reviews*, 108(11), 4784-4822.
- 607 Rudolph, W. W., Michels, M. R., & Pye, C. C. (2004). Raman, infrared, and ab initio
608 investigation of HPO₄²⁻(aq). *Science Access*, 2(1), 360-361.

- 609 Ruiz-Agudo, E., & Putnis, C. V. (2012). Direct observations of mineral-fluid reactions using
610 atomic force microscopy: the specific example of calcite. *Mineralogical Magazine*, 76(1),
611 227-253.
- 612 Ruiz-Agudo, E., Kowacz, M., Putnis, C. V., & Putnis, A. (2010). The role of background
613 electrolytes on the kinetics and mechanism of calcite dissolution. *Geochimica et*
614 *cosmochimica acta*, 74(4), 1256-1267.
- 615 Ruiz-Agudo, E., Putnis, C. V., Jiménez-López, C., & Rodríguez-Navarro, C. (2009). An atomic
616 force microscopy study of calcite dissolution in saline solutions: The role of magnesium
617 ions. *Geochimica et Cosmochimica Acta*, 73(11), 3201-3217.
- 618 Schott, J., Brantley, S., Crerar, D., Guy, C., Borcsik, M., & Willaime, C. (1989). Dissolution
619 kinetics of strained calcite. *Geochimica et Cosmochimica Acta*, 53(2), 373-382.
- 620 Shiraki, R., Rock, P. A., & Casey, W. H. (2000). Dissolution kinetics of calcite in 0.1 M NaCl
621 solution at room temperature: an atomic force microscopic (AFM) study. *Aquatic*
622 *Geochemistry*, 6(1), 87-108.
- 623 Sjöberg, E. L. (1976). A fundamental equation for calcite dissolution kinetics. *Geochimica et*
624 *Cosmochimica Acta*, 40(4), 441-447.
- 625 Sjöberg, E. L., & Rickard, D. T. (1984). Temperature dependence of calcite dissolution kinetics
626 between 1 and 62 C at pH 2.7 to 8.4 in aqueous solutions. *Geochimica et Cosmochimica*
627 *Acta*, 48(3), 485-493.
- 628 Sjöberg, E. L., & Rickard, D. T. (1985). The effect of added dissolved calcium on calcite
629 dissolution kinetics in aqueous solutions at 25 C. *Chemical geology*, 49(4), 405-413.
- 630 Smith, M. E., Knauss, K. G., & Higgins, S. R. (2013). Effects of crystal orientation on the
631 dissolution of calcite by chemical and microscopic analysis. *Chemical Geology*, 360, 10-
632 21.
- 633 Song, J., Zeng, Y., Wang, L., Duan, X., Puerto, M., Chapman, W. G., ... & Hirasaki, G. J. (2017).
634 Surface complexation modeling of calcite zeta potential measurements in brines with
635 mixed potential determining ions (Ca^{2+} , CO_3^{2-} , Mg^{2+} , SO_4^{2-}) for characterizing carbonate
636 wettability. *Journal of colloid and interface science*, 506, 169-179.
- 637 Stack, A. G., & Grantham, M. C. (2010). Growth rate of calcite steps as a function of aqueous
638 calcium-to-carbonate ratio: independent attachment and detachment of calcium and
639 carbonate ions. *Crystal Growth & Design*, 10(3), 1409-1413.

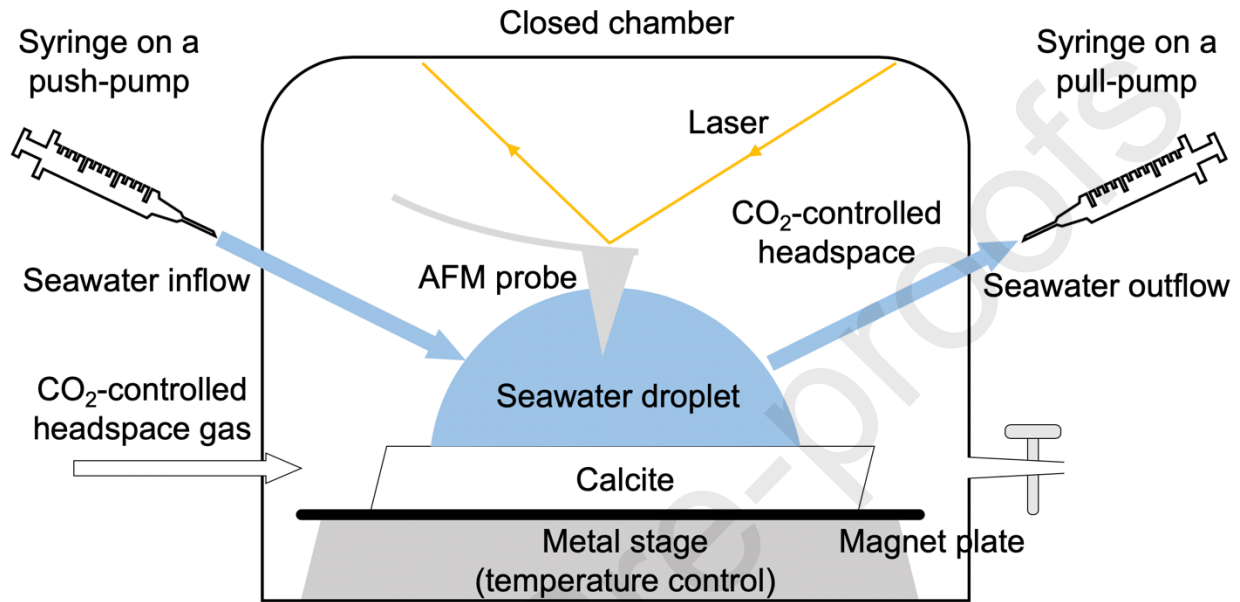
- 640 Steefel, C. I., & Van Cappellen, P. (1990). A new kinetic approach to modeling water-rock
641 interaction: The role of nucleation, precursors, and Ostwald ripening. *Geochimica et*
642 *Cosmochimica Acta*, 54(10), 2657-2677.
- 643 Stipp, S. L. S., Eggleston, C. M., & Nielsen, B. S. (1994). Calcite surface structure observed at
644 microtopographic and molecular scales with atomic force microscopy
645 (AFM). *Geochimica et Cosmochimica Acta*, 58(14), 3023-3033.
- 646 Stranski, I. N. (1928). Zur theorie des kristallwachstums. *Zeitschrift für physikalische*
647 *Chemie*, 136(1), 259-278.
- 648 Subhas, A. V., Adkins, J. F., Rollins, N. E., Naviaux, J., Erez, J., & Berelson, W. M. (2017).
649 Catalysis and chemical mechanisms of calcite dissolution in seawater. *Proceedings of the*
650 *National Academy of Sciences*, 114(31), 8175-8180.
- 651 Subhas, A. V., Rollins, N. E., Berelson, W. M., Dong, S., Erez, J., & Adkins, J. F. (2015). A
652 novel determination of calcite dissolution kinetics in seawater. *Geochimica et*
653 *Cosmochimica Acta*, 170, 51-68.
- 654 Teng, H. H. (2004). Controls by saturation state on etch pit formation during calcite
655 dissolution. *Geochimica et Cosmochimica Acta*, 68(2), 253-262.
- 656 Teng, H. H., & Dove, P. M. (1997). Surface site-specific interactions of aspartate with calcite
657 during dissolution: Implications for biomineralization. *American Mineralogist*, 82(9-10),
658 878-887.
- 659 Teng, H. H., Chen, Y., & Pauli, E. (2006). Direction specific interactions of 1, 4-dicarboxylic
660 acid with calcite surfaces. *Journal of the American Chemical Society*, 128(45), 14482-
661 14484.
- 662 Uppström, L. R. (1974). The boron/chlorinity ratio of deep-sea water from the Pacific Ocean.
663 *In Deep Sea Research and Oceanographic Abstracts* (Vol. 21, pp. 161-162).
- 664 Van Driessche, A. E., García-Ruiz, J. M., Delgado-López, J. M., & Sazaki, G. (2010). In situ
665 observation of step dynamics on gypsum crystals. *Crystal growth & design*, 10(9), 3909-
666 3916.
- 667 Van Heuven, S. M. A. C., Pierrot, D., Rae, J. W. B., Lewis, E., & Wallace, D. W. R. (2011).
668 MATLAB program developed for CO₂ system calculations. *ORNL/CDIAC-105b. Carbon*
669 *Dioxide Information Analysis Center, Oak Ridge National Laboratory, US Department of*
670 *Energy, Oak Ridge, Tennessee, 530.*

- 671 Vinson, M. D., & Lüttge, A. (2005). Multiple length-scale kinetics: an integrated study of calcite
672 dissolution rates and strontium inhibition. *American Journal of Science*, 305(2), 119-146.
- 673 Vinson, M. D., Arvidson, R. S., & Lüttge, A. (2007). Kinetic inhibition of calcite (1 0 4)
674 dissolution by aqueous manganese (II). *Journal of Crystal Growth*, 307(1), 116-125.
- 675 Wolthers, M., Nehrke, G., Gustafsson, J. P., & Van Cappellen, P. (2012). Calcite growth kinetics:
676 Modeling the effect of solution stoichiometry. *Geochimica et Cosmochimica Acta*, 77,
677 121-134.
- 678 Xu, J., Fan, C., & Teng, H. H. (2012). Calcite dissolution kinetics in view of Gibbs free energy,
679 dislocation density, and pCO₂. *Chemical Geology*, 322, 11-18.
- 680 Xu, M., & Higgins, S. R. (2011). Effects of magnesium ions on near-equilibrium calcite
681 dissolution: Step kinetics and morphology. *Geochimica et Cosmochimica Acta*, 75(3),
682 719-733.
- 683 Xu, M., Hu, X., Knauss, K. G., & Higgins, S. R. (2010). Dissolution kinetics of calcite at 50–70°
684 C: An atomic force microscopic study under near-equilibrium conditions. *Geochimica et*
685 *Cosmochimica Acta*, 74(15), 4285-4297.
- 686 Yuan, K., Starchenko, V., Lee, S. S., De Andrade, V., Gursoy, D., Sturchio, N. C., & Fenter, P.
687 (2019). Mapping three-dimensional dissolution rates of calcite microcrystals: Effects of
688 surface curvature and dissolved metal ions. *ACS Earth and Space Chemistry*, 3(5), 833-
689 843.
- 690 Zhang, J., & Nancollas, G. H. (1998). Kink Density and Rate of Step Movement during Growth
691 and Dissolution of an AB Crystal in a Nonstoichiometric Solution. *Journal of Colloid*
692 *and Interface Science*, 200(1), 131-145.
- 693
- 694
- 695

696

697 **Figure Caption**

698

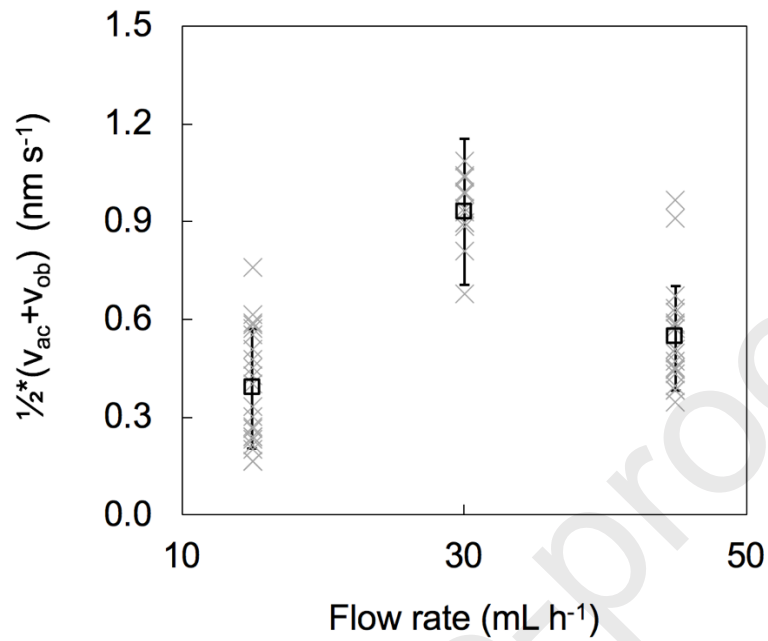


699

700 Figure 1. AFM *in situ* dissolution experiment setup.

701

702

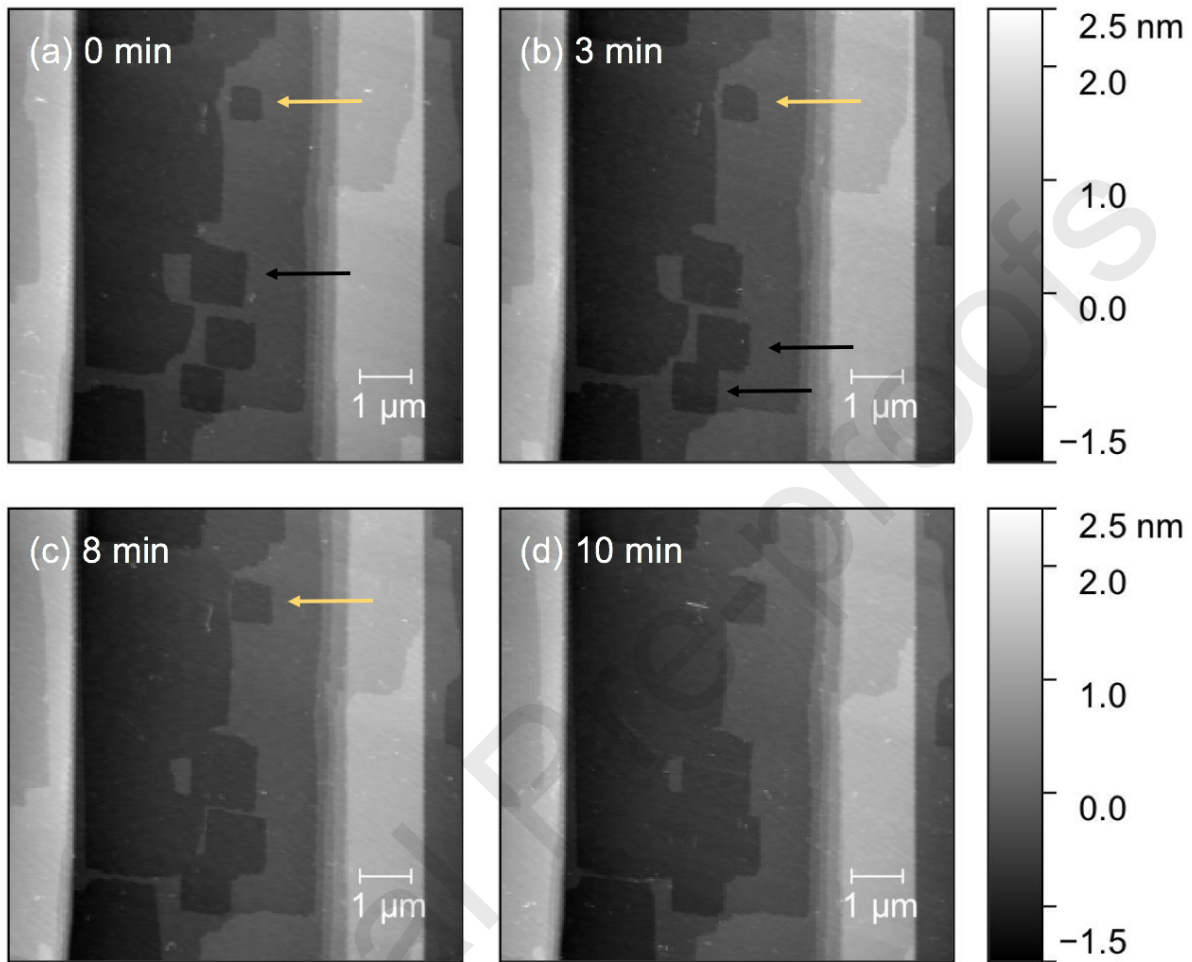


703

704 Figure 2. Average step velocity of acute and obtuse edges at three different flow rates (15 mL h⁻¹,
705 30 mL h⁻¹, 45 mL h⁻¹) at $\Omega = 0.37 \pm 0.01$. The grey crosses are velocities at different individual
706 etch pits. The squares are the mean values of the crosses, with the error bars representing one
707 standard deviation of the population.

708

709

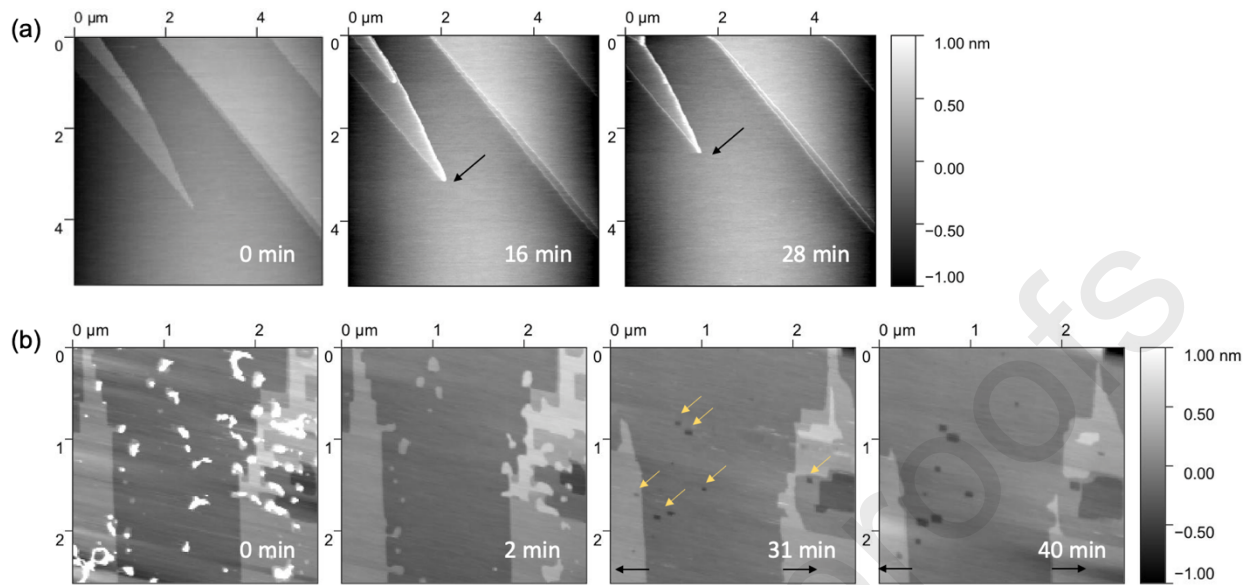


710

711 Figure 3. One example of dissolution on the calcite {104} cleavage surface in seawater ($\Omega =$
 712 0.46 ± 0.01). 0 min in Figure 3a is actually 37 min after the start of the continuous seawater
 713 flow.

714

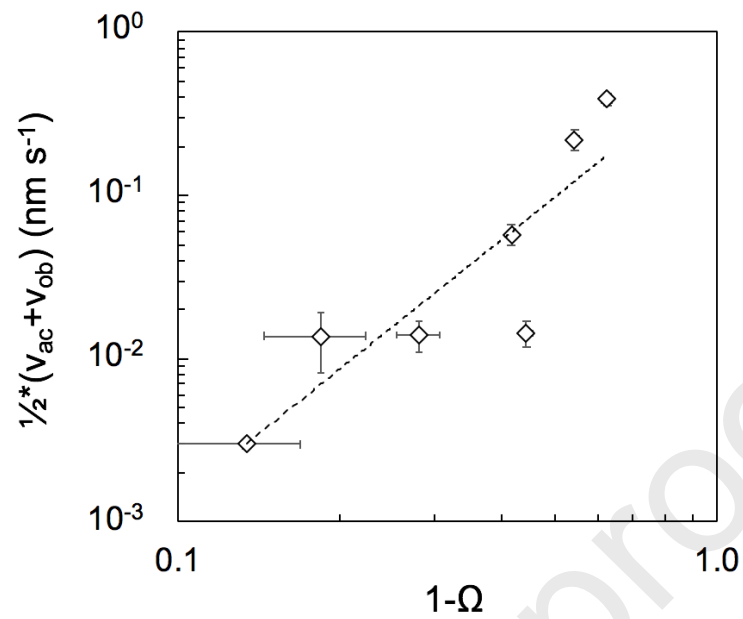
715



716

717 Figure 4. (a) $\Omega = 0.88 \pm 0.04$; (b) $\Omega = 0.50 \pm 0.02$ (etch pits formed before $t=31$ min, but
 718 image quality was poor). At $\Omega = 0.88 \pm 0.04$, dissolution only happens as step retreat (black
 719 arrows). No etch pit formation was found for 30 min within the total scanned area of $17.04 \mu\text{m}$
 720 $\times 17.04 \mu\text{m}$. At $\Omega = 0.50 \pm 0.02$, dissolution happens both at existing step edges (black arrows)
 721 and at newly-formed etch pits (yellow arrows). The highest Ω observed for etch pit formation is
 722 0.82 ± 0.04 with a pit density of $3.1 \times 10^6 \text{ cm}^{-2}$.

723



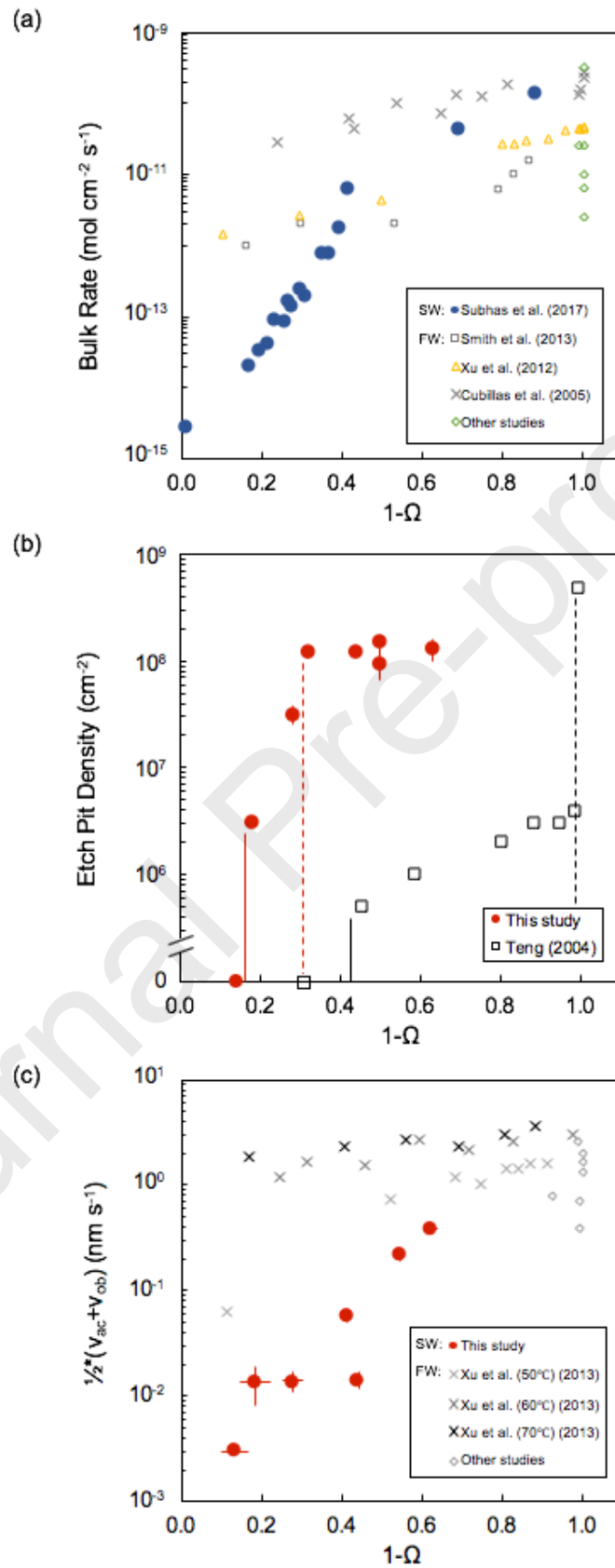
724

725 Figure 5. Average step velocity of acute and obtuse edges vs. undersaturation. Note that this is a

726 log-log plot, so the slope of 2.6 indicates that the correlation is a power function with an order of

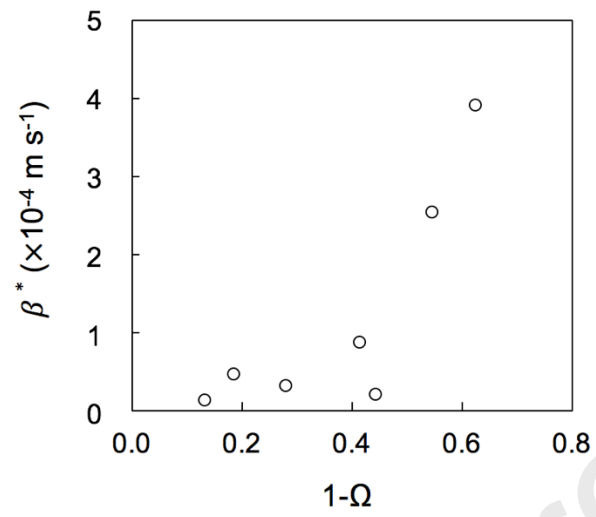
727 2.6.

728



730 Figure 6. Comparisons of (a) bulk dissolution rate, (b) etch pit density and (c) step velocity
731 between dissolution in seawater (SW) and in low ionic strength water (FW for freshwater). In 6b,
732 the solid and dashed lines represent the transitions of the dominating surface dissolution
733 mechanism, for seawater (red) and low ionic water (black) respectively. Solid lines are the
734 Ω_{critical} between step retreat and defect-assisted etch pit formation. Dashed lines are the Ω_{critical}
735 between defect-assisted and homogeneous etch pit formation. [Subhas et al. \(2017\)](#) and this study
736 are in seawater, all others are in low ionic strength water. “Other studies” in Figure 6a and 6c
737 include: [Shiraki et al., 2000](#); [De Giudici, 2002](#); [Arvidson et al., 2003](#); [Arvidson et al., 2006](#);
738 [Vinson and Lüttge, 2005](#); [Lea et al, 2001](#); [Harstad and Stipp, 2007](#). Except for [Xu et al. \(2010\)](#)
739 which has experimental temperatures of 50~70 °C, all other studies are between 20 °C and 25 °C.
740 Experimental details are listed in Table 1, 3 and 4.

741



742

743 Figure 7. Our measured “kinetic coefficient” β^* as a function of $(1-\Omega)$.

744 **Table Caption**

745 Table 1. Average of acute and obtuse step velocities against saturation states

746

Expt. No.	DIC ($\mu\text{mol kg}^{-1}$)	Alkalinity ($\mu\text{mol kg}^{-1}$)	Ω	No. of v in the population statistics	$\frac{1}{2} * (v_{ac} + v_{ob})$ (nm s^{-1})
AF-3	2025.0 ± 3.5	1922.9 ± 0.9	0.46 ± 0.01	16	0.219 ± 0.031
AF-5	2027.8 ± 0.9	1960.3 ± 0.6	0.58 ± 0.01	9	0.0577 ± 0.0086
AF-7	2024.8 ± 10.1	1984.4 ± 0.4	0.72 ± 0.03	7	0.0140 ± 0.0031
AF-9	2021.3 ± 5.8	1997.2 ± 2.5	0.82 ± 0.04	2	0.0137 ± 0.0055
AF-18	2015.1 ± 2.1	1942.4 ± 1.9	0.56 ± 0.01	10	0.0143 ± 0.0025
AF-20	2064.3 ± 6.4	1926.3 ± 2.8	0.37 ± 0.01	22	0.388 ± 0.037
AF-8	2021.3 ± 5.8	1997.2 ± 2.5	0.87 ± 0.04	3	0.00298 ± 0.00019

747

748

749
750
751

Table 2. Published effects of different ions on calcite dissolution and the ion concentrations in Dickson standard seawater

Ion	Effect(s) on dissolution	Minimum concentration for the effect(s) (mol kg ⁻¹)	Concentration in Dickson standard seawater (mol kg ⁻¹)	Reference
CO ₃ ²⁻	Etch pit morphology, step velocity	1.5×10^{-4} (*)	2.6×10^{-5}	Lea et al. (2001)
PO ₄ ³⁻	Etch pit morphology and density, step velocity	10^{-3}	2.9×10^{-7}	Klasa et al. (2013)
Mn ²⁺	Etch pit morphology, step velocity	1.0×10^{-6}	3.6×10^{-10}	Lea et al. (2001); Vinson et al., 2007
Mg ²⁺	Etch pit morphology, density, and depth, step velocity	$10^{-5} \sim 10^{-3}$	5×10^{-2}	Arvidson et al. (2006); Ruiz-Agudo et al. (2009); Xu and Higgins (2010)
SO ₄ ²⁻	Etch pit density, depth, step velocity	10^{-1}	3×10^{-2}	Ruiz-Agudo et al. (2009)
Sr ²⁺	Step velocity (slightly)	5×10^{-6}	9×10^{-5}	Lea et al. (2001)

752
753

* indicates that the concentration is the minimum addition in the study

754
755
756

Table 3. A comparison of bulk rate and step velocity between this study and previous publications.

Log bulk rate (mol cm ⁻² s ⁻¹)	Step velocity (nm/s)	(v _o +v _a)/2 (nm/s)	Material	Solution	Ω _{calcite}	pH	T (°C)	Method	Reference
-14.1 ~ -11.9	N.A.	0.003~0.4	Iceland Spar (104) surface	Natural seawater	0.4 ~ 0.9	7.0-7.3	21	AFM	This study
-14.5 ~ -9.9	N.A.	N.A.	Calcite powder	Natural seawater	0.02 ~ 0.99	5.9-7.3	21	Bulk dissolution	Subhas et al. (2017)
-13.0 ~ -10.4	N.A.	N.A.	Iceland Spar	NaCl-NaHCO ₃ - CaCl ₂ solution	0.1 ~ 0.8	8.0-8.1	20	VSI and bulk dissolution	Smith et al. (2013)
-12.0 ~ -10.2	N.A.	N.A.	Fragmental and powder samples	NaHCO ₃ -CaCl ₂ solution	10 ⁻⁴ ~ 0.9	>8	25	Bulk dissolution	Xu et al. (2012)
-9.8	N.A.	N.A.	Calcite powder	HCl solution	10 ⁻³	7.3	25	Bulk dissolution	Cubillas et al. (2005)
N.A.	v _o =0~3; v _a =0~0.6	0~1.7	Iceland Spar (104) surface	NaCl-NaHCO ₃ - CaCl ₂ solution	0.09 ~ 1.2	7.8-8.3	50	AFM	Xu et al. (2010)
-9.5	v _o =3; v _a =1	2	Iceland Spar (104) surface	NaCl solution	10 ⁻⁷	7.6	21	AFM	Shiraki et al. (2000)
N.A.	v _o =0.90; v _a =0.67	0.79	Iceland Spar (104) surface	Na ₂ CO ₃ solution	0.07	8.9	22	AFM	Lea et al. (2001)
-10.6	v _o =4.2; v _a =0.9	2.6	Iceland Spar (104) surface	HCl solution	10 ^{-2.15}	7.5	22	AFM	De Giudici (2002)
-11.0	0.00337	0.00337	Iceland Spar (104) surface	NaHCO ₃ - Na ₂ CO ₃ solution	10 ^{-3.41}	8.8	25	VSI	Arvidson et al. (2003)

-11.6	$v_o=0.04;$ $v_a=0.74$	0.39	Iceland Spar (104) surface	NaHCO ₃ solution	10 ^{-3.39}	8.8	25	VSI, AFM	Arvidson et al. (2006)
-11.2	$v_o=0.27;$ $v_a=1.14$	0.71	Iceland Spar (104) surface	Na ₂ CO ₃ solution	10 ^{-3.59}	8.7	22	VSI, AFM	Vinson and Lüttge (2005)
-10.6	$v_o=1.98;$ $v_a=1.51$	1.75		NaCl solution	N.A.	8.6			
N.A.	$v_o=0.29\sim 2.10;$ $v_a=0.19\sim 0.55$	0.24~1.3	Iceland Spar (104) surface	Milli-Q water	N.A.	5.6-8.3	30	AFM	Harstad and Stipp (2007)

757

758 * Except for this study and [Subhas et al. \(2017\)](#), all other studies in Table 3 are considered as low ionic strength water studies (Milli-Q

759 water w/wo addition of certain ions).

Table 4. Measured etch pit density against solution undersaturation.

Expt. No.	DIC ($\mu\text{mol kg}^{-1}$)	Alkalinity ($\mu\text{mol kg}^{-1}$)	Ω	Average etch pit numbers	Error etch pit numbers	Image area (μm^2)	Average etch pit density (cm^{-2})	Error etch pit density (cm^{-2})
AF-9	2021.3 ± 5.8	1997.2 ± 2.5	0.82 ± 0.04	1	0	31.9	3.1×10^6	0
AF-14	2023.1 ± 10.1	1982.5 ± 1.7	0.72 ± 0.05	10	2	31.6	3.2×10^7	6.3×10^6
AF-17	2010.4 ± 9.6	1964.3 ± 0.3	0.68 ± 0.05	17	2	13.9	1.2×10^8	1.4×10^7
AF-18	2015.1 ± 2.1	1942.4 ± 1.9	0.56 ± 0.01	8	0	6.4	1.2×10^8	0
AF-11	2030 ± 10	1940 ± 2	0.50 ± 0.05	9	3	9.2	9.8×10^7	3.3×10^7
AF-12	2032.9 ± 4.3	1942.5 ± 2.2	0.50 ± 0.02	23	3	14.7	1.5×10^8	1.7×10^7
AF-20	2064.3 ± 6.4	1926.3 ± 2.8	0.37 ± 0.01	33	8	25.0	1.3×10^8	3.0×10^7
Teng	N.A.	N.A.	0.012~0.54	N.A.	N.A.	N.A.	$<4 \times 10^6$	N.A.
(2004)	N.A.	N.A.	0.007	N.A.	N.A.	N.A.	5×10^8	N.A.

762 * Error in etch pit numbers is determined by the variation between images at different time.

Supplementary Materials

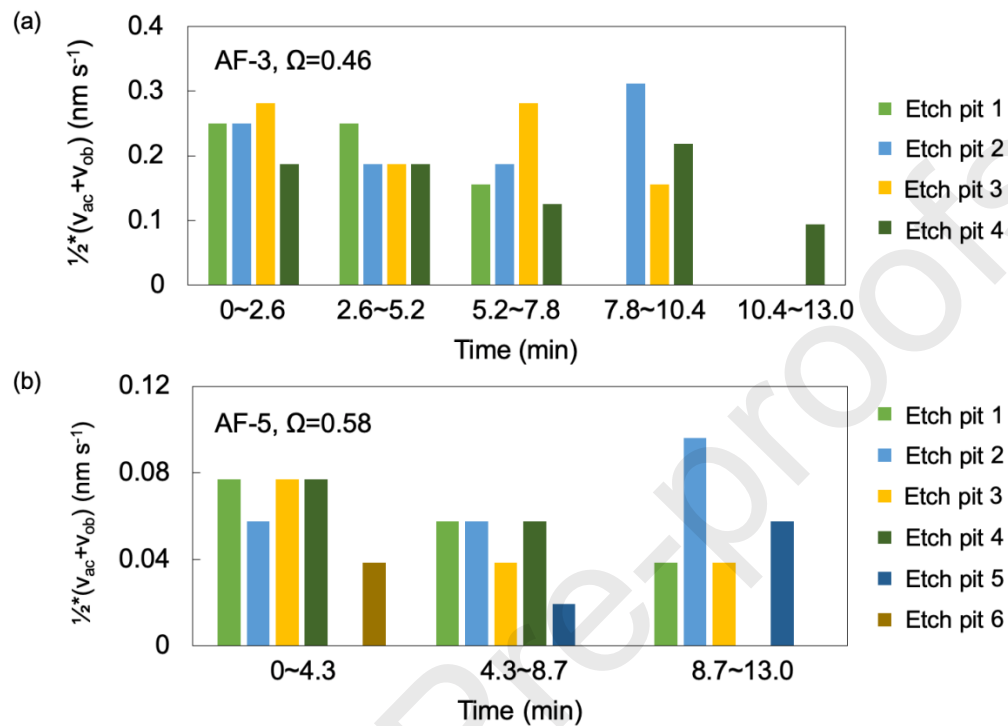


Figure S1. Step velocities of individual etch pits during different time periods for two experiments. Measured step velocities are independent of time and etch pit location. The variation is largely due to the limited precision in width measurement.

Table S1 Chemical composition of Dickson standard seawater Batch 176.

Salinity	33.532
DIC	2024.22±0.82 $\mu\text{mol kg}^{-1}$
Phosphate	0.29 $\mu\text{mol kg}^{-1}$
Silicate	1.7 $\mu\text{mol kg}^{-1}$
Nitrite	0.01 $\mu\text{mol kg}^{-1}$
Nitrate	0.8 $\mu\text{mol kg}^{-1}$

Table S2. DIC, alkalinity and Ω of the fill bag, solution in inflow syringe and solution in outflow syringe.

	DIC ($\mu\text{mol kg}^{-1}$)	No. of DIC samples	DIC std error ($\mu\text{mol kg}^{-1}$)	Alkalinity ($\mu\text{mol kg}^{-1}$)	No. of alk. samples	Alk. std error ($\mu\text{mol kg}^{-1}$)	Ω	Ω error
Fill bag	2125.2	2	10.0	1989.2	3	0.95	0.398	0.021
Inflow solution	2139.4	1	N.A. (15) *	1989.6	1	N.A. (2) *	0.373	0.028
Outflow solution	2145.8	3	16.8	1993.8	2	0.45	0.370	0.031

* Standard errors not available because there was only enough sample for single DIC and alkalinity measurement. Errors in the parenthesis were used to calculate the error of Ω .

Abbreviations: No. = number; std = standard; alk. = alkalinity; N.A. = not available.